

Reconstructing Galaxy Cluster Mass Maps using Score-based Generative Modeling

ALAN HSU,^{1,2} MATTHEW HO,^{3,4} JOYCE LIN,^{5,2} CARLEEN MARKEY,^{2,6} MICHELLE NTAMPAKA,^{7,8} HY TRAC,^{2,6} AND BARNABÁS PÓCZOS⁹

¹*Department of Astronomy, Harvard University, Cambridge, MA 02138, USA*

²*Department of Physics, Carnegie Mellon University, Pittsburgh, PA 15213, USA*

³*CNRS & Sorbonne Université, Institut d'Astrophysique de Paris (IAP), UMR 7095, 98 bis bd Arago, F-75014 Paris, France*

⁴*Columbia Astrophysics Laboratory, Columbia University, 550 West 120th Street, New York, NY 10027, USA*

⁵*Department of Physics, University of Wisconsin-Madison, Madison, Wisconsin 53726, USA*

⁶*McWilliams Center for Cosmology and Astrophysics, Carnegie Mellon University, Pittsburgh, PA 15213, USA*

⁷*Data Science Mission Office, Space Telescope Science Institute, Baltimore, MD, 21218, USA*

⁸*Department of Physics & Astronomy, Johns Hopkins University, Baltimore, MD 21218, USA*

⁹*Machine Learning Department, Carnegie Mellon University, Pittsburgh, PA 15213, USA*

Submitted to The Open Journal of Astrophysics

ABSTRACT

We present a novel approach to reconstruct gas and dark matter projected density maps of galaxy clusters using score-based generative modeling. Our diffusion model takes in mock SZ and X-ray images as conditional inputs, and generates realizations of corresponding gas and dark matter maps by sampling from a learned data posterior. We train and validate the performance of our model by using mock data from a hydrodynamical cosmological simulation. The model accurately reconstructs both the mean and spread of the radial density profiles in the spatial domain to within 5%, indicating that the model is able to distinguish between clusters of different sizes. In the spectral domain, the model achieves close-to-unity values for the bias and cross-correlation coefficients, indicating that the model can accurately probe cluster structures on both large and small scales. Our experiments demonstrate the ability of score models to learn a strong, nonlinear, and unbiased mapping between input observables and fundamental density distributions of galaxy clusters. These diffusion models can be further fine-tuned and generalized to not only take in additional observables as inputs, but also real observations and predict unknown density distributions of galaxy clusters.

1. INTRODUCTION

Galaxy clusters are the largest gravitationally bound systems in the universe, typically comprised of hundreds of galaxies and a hot intracluster medium (ICM) embedded in a dark matter halo. The cluster mass scales with galaxy velocity dispersion, a relation famously used to postulate the presence of dark matter in the Coma cluster (Zwicky 1933). The number density of galaxy clusters as a function of their mass is a cosmological probe, and is sensitive to the distribution and evolution of large-scale structures in the cosmic web. See Allen et al. (2011) and Kravtsov & Borgani (2012) for reviews.

The primary baryonic component of galaxy clusters is the ICM, a hot, ionized gas that is observable over a range of wavelengths. The plasma radiates through thermal bremsstrahlung (free-free) emission at X-ray energies. The free electrons upscatter the cosmic microwave background (CMB) through the Sunyaev-Zel'dovich (SZ, Sunyaev & Zeldovich 1972) effect and is detected at microwave frequencies. Observations of the ICM can be used as a mass proxy, a way to infer the underlying mass from observables, and both X-ray (e.g. Vikhlinin et al. 2006; Pratt et al. 2009; Mantz et al. 2016; Giles et al. 2017) and SZ (e.g. Marriage et al. 2011; Reichardt et al. 2013; Hilton et al. 2021; Melin et al. 2021; Bleem et al. 2024) observations of clusters have been utilized in this way. These mass proxies may either be derived from first principles or calibrated on

cluster simulations (e.g. Kravtsov et al. 2006; Kay et al. 2012; Wadekar et al. 2023a).

Recently, machine learning models have been shown to improve standard estimates of galaxy cluster mass, using observables such as line-of-sight velocities and projected radial distances (e.g. Ho et al. 2019; Kodi Ramanaiah et al. 2020, 2021; Ho et al. 2021, 2022), X-ray (e.g. Ntampaka et al. 2019; Green et al. 2019; Han et al. 2020; Ho et al. 2023) and SZ (e.g. Cohn & Battaglia 2019; Wadekar et al. 2023b). However, compared to standard estimates of cluster mass, estimating the projected 2D mass map is even more informative: knowing the mass map at different radii not only estimates cluster abundance but also better constrains lensing maps and dark matter models. Finally, since clusters effectively act as giant telescopes to magnify and find high redshift galaxies and quasars, having a model that accurately produces the mass map is crucial. To do so, we will need a machine learning model that can produce images rather than single-number estimates for the mass.

Concurrently, image-to-image deep learning models have been used to effectively model galaxy cluster structures by learning a compressed latent space representation and sampling from a learned distribution. These generative models compress the input into a latent space by extracting the most useful information that is further used to sample outputs, capturing and appropriately modeling the intrinsic uncertainty in incomplete observations. Examples of reconstruction from the latent space include random sampling of hyper-realistic large cosmological structures (e.g. Ullmo et al. 2021), and accurate reconstruction of galaxy images (e.g. Schawinski et al. 2018) and large-scale structures (e.g. Rodriguez et al. 2018; Perraudin et al. 2019). Other interesting applications of image generation include reconstructing dark matter maps from cluster observables (e.g. de Andres et al. 2024), classification of galaxy mergers (e.g. Arendt et al. 2024), denoising and deconvolving galaxy images (e.g. Schawinski et al. 2017; Hemmati et al. 2022) and increasing the resolution of cosmological simulations (e.g. Li et al. 2021).

A recent paradigm shift in image-to-image generative modeling is the development of diffusion or score-based generative modeling, which is a probabilistic framework that reformulates the previous sampling processes from learned data distributions. By increasingly injecting noise into our data and learning the inverse denoising procedure, we can map a prior distribution to the data distribution and subsequently sample from it. Score matching with Langevin Dynamics (SMLD, e.g. Vincent 2011; Song & Ermon 2019; Song et al. 2021) learns the score, or the gradient of the log probability den-

sity, of the data distribution which is used by Langevin dynamics to generate data using stochastic differential equations (SDEs). An analogous score-based framework is Denoising Diffusion Probabilistic Modeling (DDPM, e.g. Sohl-Dickstein et al. 2015; Ho et al. 2020) which implicitly learns the score by training a sequence of models to reverse the noise injection. In the context of astrophysics generative modeling, this probabilistic framework can learn and sample images from posterior distributions rather than points estimates: recent work in astrophysics has been applied to a variety of tasks, including sampling galaxy spectra (e.g. Doorenbos et al. 2022, 2024), super-resolution gravitational lensing maps (e.g. Reddy et al. 2024), satellite galaxies and subhalo populations (e.g. Nguyen et al. 2024; Bourdin et al. 2024), and initial conditions of the universe (e.g. Legin et al. 2023).

We present a score-based generative model that learns the predictive posterior distribution of gas and dark matter maps of galaxy clusters. This powerful probabilistic modeling allows us to subsequently sample realizations of these maps conditioned on SZ and X-ray inputs. In Section 2, we detail the process of generating mock observations from a large hydrodynamical simulation as training and testing data for our models. In section 3, we describe the diffusion model pipeline and elaborate on the statistical framework of learning the score of the data distribution. Finally, in section 4 we present the estimated gas and dark matter maps, the reconstructed accuracy of the density profiles in the spatial domain, and the bias and cross correlation coefficients in the spectral domain.

2. SIMULATIONS

We apply score-based generative modeling on simulated galaxy clusters to study its potential for reconstructing the underlying mass maps. With simulated galaxy clusters, we know the gas and dark matter properties and distributions and can construct corresponding multi-wavelength mock observations. This important, pilot step to quantify the accuracy and uncertainties with simulated images is necessary before the approach can be applied to real observations. In this section, we first describe the cosmological simulation (Section 2.1) and galaxy cluster sample (Section 2.2). We then describe the construction of mock observations of the SZ effect (Section 2.3) and X-ray emission (Section 2.4).

2.1. Cosmological Simulation

Many supervised machine learning models, such as the image-to-image diffusion model that will be described in Section 3, require large amounts of data for training.

We generate a large number of simulated galaxy clusters by running a cosmological simulation of galaxy clusters with an updated version of HYPER (He et al. 2022), a hydro-particle code for efficient and rapid simulations of baryons and dark matter. The hydro simulation used here has a moderately large volume so as to produce many galaxy clusters, paired with a high enough resolution to model internal cluster structures. This combination of large volume and high resolution is made possible due to the novel approach of subgrid models for the thermodynamics of the ICM and IGM, which results in three orders of magnitude speedup compared to a standard hydrodynamics code. In particular, we use an ICM pressure profile and IGM temperature-density relation, both of which can be systematically varied for parameter space studies, and these facilitate the creation of mock X-ray and SZ observations from the simulated ICM.

For the gravity solver, the particle-mesh (PM) algorithm is upgraded to particle-particle-mesh (P³M; Trac et al. 2015) for improved spatial resolution. For the hydro solver, some components of the hydro-particle-mesh (HPM; Gnedin & Hui 1998; He et al. 2022) algorithm are replaced with elements from smoothed particle hydrodynamics (SPH; see Springel 2010, for a review). Particle densities and pressure gradients are not calculated using a mesh, but rather by summing over and weighting particles within the individual smoothing lengths. The kick-drift-kick leapfrog integrator now uses adaptive time steps for improved efficiency. The subgrid model for the intracluster medium (ICM) is based on the debiased pressure profile (DPP; He et al. 2021), which adjusts for hydrostatic mass bias by combining results from X-ray observations (e.g. Böhringer et al. 2007) with cosmological simulations (e.g. Barnes et al. 2021).

The simulation is based on the following cosmological parameters: $\Omega_b = 0.045$, $\Omega_m = 0.3$, $\Omega_\Lambda = 0.7$, $h = 0.7$, $\sigma_8 = 0.8$, and $n_s = 0.96$. There are $N_{\text{dm}} = 1024^3$ dark matter particles and $N_{\text{gas}} = 1024^3$ gas particles in a comoving box of side length $L_{\text{sim}} = 500 h^{-1}\text{Mpc}$. The particle masses are $m_{\text{dm}} = 1.18 \times 10^{10} M_\odot$ and $m_{\text{gas}} = 2.08 \times 10^9 M_\odot$, and the gravitational softening length is $\epsilon = 44$ kpc. A spherical overdensity halo finder is used to locate halos with density equal to 200 times the average matter density. The halo mass function is accurate to $\lesssim 5\%$ for halos with $\gtrsim 200$ (gas and dark matter) particles. The simulation was run on the NASA Endeavour supercomputer using 256 cores and taking only 9000 CPU-hours.

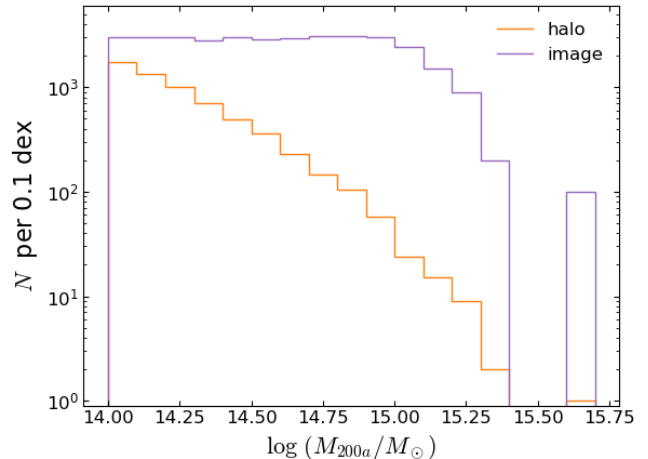


Figure 1. The number of massive clusters (orange) decreases exponentially in the high-mass tail of the halo mass function. From these simulated clusters, we generate mock images (purple) to maintain approximately 3000 per 0.1 dex in mass except at the very highest masses, resulting in a uniform mass prior to avoid biases in training.

2.2. Galaxy Cluster Sample

The HYPER simulation described above produces 6,233 galaxy clusters at redshift $z = 0$. The smallest halo has mass $M_{200a} = 1.00 \times 10^{14} M_\odot$ and is resolved with ~ 14000 particles within a radius $R_{200a} = 1.44$ Mpc. The largest halo has $M_{200a} = 4.82 \times 10^{15} M_\odot$ and contains $\sim 700,000$ particles within $R_{200a} = 5.21$ Mpc. Figure 1 shows that the number of halos decreases exponentially in the high-mass tail of the distribution. To avoid biases in the ML model, we create a flat distribution with logarithmic mass (e.g. Ntampaka et al. 2015; Ho et al. 2019). For the higher-mass clusters, we generate more sightlines by rotating the particle coordinates. For the lower-mass clusters, we subsample if necessary.

For a given cluster sightline, we first construct three-dimensional fields such as density and pressure by mapping the particles onto a Cartesian mesh with side length of 12.8 Mpc, which is slightly larger than the diameter of the largest halo. For a given field, we then project along up to three cardinal axes to make two-dimensional images with pixel size $l_{\text{pixel}} = 100$ kpc and $N_{\text{pixel}} = 128$ pixels per side length. The pixel size is approximately twice the gravitational softening length and comparable to the effective resolution of the HYPER simulation. The image resolution is comparable to current X-ray observations and to followup SZ observations. Figure 1 shows that the number of images generated is flat with approximately 3000 per 0.1 dex in mass, except at the very highest masses where we impose a maximum number of sightlines per cluster.

Following the SPH approach, the density field for particle species $x = \text{Gas, DM}$ is calculated using a weighted summation over nearby particles j with mass m_j and smoothing length h_j :

$$\rho_x(\mathbf{r}) = \sum_j m_j W(\mathbf{r} - \mathbf{r}_j, h_j). \quad (1)$$

The smoothing kernel is chosen to be a Wendland function (e.g. [Dehnen & Aly 2012](#)),

$$W(q, h) = \frac{21}{2\pi h^3} (1 - q)^4 (1 + 4q), \quad (2)$$

where $q = r/h \in [0, 1]$, consistent with that used in the HYPER simulation. Other fields like the gas pressure are calculated similarly to Eq. 1 (see [Springel 2010](#), for a review).

We calculate the normalized projected density for component $x = \text{Gas, DM}$ by integrating the density field along a given direction:

$$S_x[i, j] = \frac{\int \rho_x(\mathbf{r}) dl}{\int \bar{\rho}_x dl} = \frac{\sum_k \rho_x[i, j, k] l_{\text{pixel}}}{\sum_k \bar{\rho}_x l_{\text{pixel}}}, \quad (3)$$

where $\bar{\rho}_x = \Omega_x \rho_{\text{crit}}$ is the cosmic average density. We make up to three projected density images for a given density field by summing the array $\rho_x[i, j, k]$ along each of the three cardinal axes and multiplying by the pixel length.

2.3. Sunyaev-Zel'dovich Effect

The Sunyaev-Zel'dovich (SZ) effect arises when cosmic microwave background (CMB) photons are scattered by ionized electrons in the ICM and IGM ([Sunyaev & Zeldovich 1970, 1972](#)). Being the dominant secondary temperature anisotropy on arcminute scales, it is a promising probe of the growth of structure. Examples include direct detection of galaxy clusters, autocorrelation of temperature fluctuations, and cross-correlation with large-scale structure.

The SZ effect is commonly considered to have two main components. The thermal SZ (TSZ) effect arises from inverse Compton scattering of the CMB with hot electrons, while the kinetic SZ (KSZ) effect is a Doppler term due to scattering with fast electrons. In this paper, we are interested in the TSZ effect from the ICM. The CMB temperature fluctuations $\Delta T/T_{\text{cmb}}$ are related to the Compton y parameter multiplied by a frequency-dependent function. The Compton y parameter is proportional to the integrated electron pressure along a given sightline,

$$y = \frac{\sigma_T}{m_e c^2} \int P_e(\mathbf{r}) dl. \quad (4)$$

For a given electron pressure field $P_e(\mathbf{r})$, we make up to three Compton y images with signal,

$$S_{\text{tsz}}[i, j] = T_{\text{cmb}} y[i, j], \quad (5)$$

by summing the pressure array along each of the three cardinal axes and multiplying by the pixel length. While the Compton y parameter is dimensionless, it is often multiplied by T_{cmb} to have convenient units of μK .

2.4. X-ray Emission

The ICM is a superheated plasma that radiates through thermal bremsstrahlung (free-free) emission. This emission can be detected at X-ray wavelengths using telescopes such as XMM-Newton, *Chandra*, eROSITA. The apparent X-ray luminosity of a cluster is a probe of the temperature and mass of its ICM which, under the assumption of hydrostatic equilibrium, can be directly related to the total system mass ([Ettori et al. 2019](#)). This ICM-based probe of cluster mass has been used broadly in X-ray surveys to characterize both individual systems (e.g. [Allen et al. 2002](#); [Aghanim et al. 2011](#); [Ilani et al. 2024](#)) and general population statistics (e.g. [Vikhlinin et al. 2009](#); [Lovisari et al. 2017](#); [Bahar et al. 2022](#)).

For a plasma of ionized hydrogen, helium, and metals, the bolometric emissivity or luminosity density is given by

$$l_{\text{bol}} \approx 1.4 \times 10^{-27} g_{\text{ff}} T^{1/2} n_e \sum_i z_i^2 n_i \text{ erg s}^{-1} \text{ cm}^{-3}, \quad (6)$$

where g_{ff} is the free-free gaunt factor, T is the plasma temperature, n_e is the electron number density, and z_i and n_i are the charge and number density of the various ions i (see [Sarazin 1988](#), for a review). For a given luminosity density field $l_{\text{bol}}(\mathbf{r})$, we make up to three X-ray surface brightness images with signal

$$S_{\text{xy}}[i, j] = \int l_{\text{bol}}(\mathbf{r}) dl = \sum_k l_{\text{bol}}[i, j, k] l_{\text{pixel}}, \quad (7)$$

by summing the luminosity density array $l_{\text{bol}}[i, j, k]$ along each of the three cardinal axes and then multiplying by the pixel length. The surface brightness images have units of $\text{erg s}^{-1} \text{ cm}^{-2}$.

3. MACHINE LEARNING

Our deep learning pipeline consists of two stages. First, we pre-process the mock observations and split our datasets into training and testing portions (Section 3.1). Second, we train the score model on the training dataset to reconstruct the gas and dark matter density maps conditioned on the SZ and X-ray inputs. In Section 3.2, we describe the framework of stochastic differential equations and how score models utilize Langevin dynamics sampling to learn the data distribution.

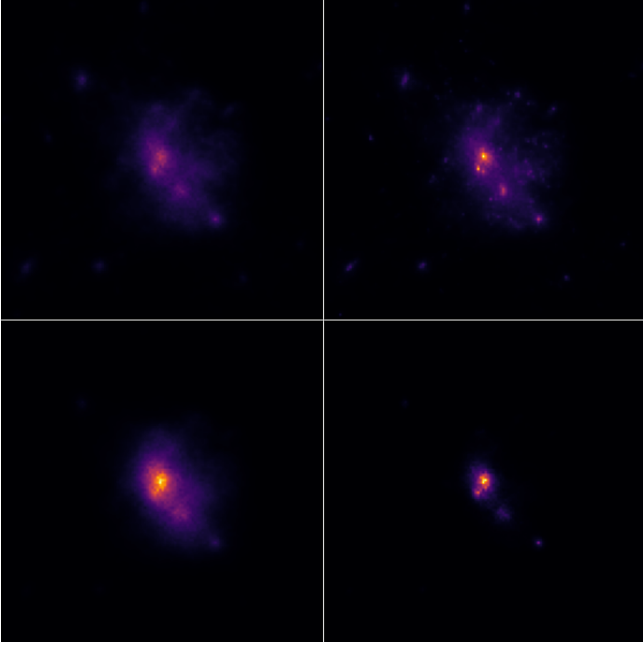


Figure 2. Simulated mass maps of gas (top left), dark matter (top right), and mock observations of SZ (bottom left), and X-ray (bottom right), of a large mass halo. The gas and dark matter are underlying distributions that we are trying to compute, while the SZ and X-ray are the observables.

3.1. Dataset Construction

Figure 2 shows sample simulation maps of gas and dark matter, and mock observations of SZ and X-ray maps of a cluster. All images are 128 by 128 pixels, with 0.1 Mpc/pixel or 12.8 Mpc in physical length. Each type of image is normalized to within 0 and 1 with the same bounds, so as to not cause large gradient updates within the network weights. Note that this operation is global: we want to preserve the relative intensities between clusters of different sizes, since we want our model to generate the mass maps with intensities associated with the input galaxy cluster size.

Our dataset consists of 34,714 sets of (SZ, X-ray, gas, dark matter) maps of galaxy clusters, which is then split into training, validation, and testing portions. We will only train our model using the training set and improve on any hyperparameters using the validation set, reserving the testing set for an unbiased evaluation of our model after the full training pipeline. In addition, while some galaxy clusters may have multiple projections in our full dataset, we ensure that all projections of each galaxy cluster are contained in exactly one of the training, validation, and testing sets. This ensures that the model does not train on any of the clusters in the test set.

3.2. Conditional Score-based Models

Our score model transforms a sample from a Gaussian random field into a realization of the gas and dark matter map of a galaxy cluster, which effectively samples from the gas and dark matter posterior distribution. Figure 3 describes the training process of a score-based model using SMLD (e.g. Song et al. 2021) using stochastic differential equations (SDEs). We provide the forward SDE to gradually transform the gas and dark matter maps into random noise, and the diffusion model learns the inverse SDE that maps the noise back to the gas and dark matter maps. In particular, the model learns to sample from the joint posterior of gas and dark matter maps of clusters conditioned on the SZ and X-ray inputs. This section discusses the statistical framework behind the sampling techniques for the posterior, and the training process for a score-based diffusion model.

We first provide a forward mapping from the final data distribution (gas and dark matter distribution) to a prior (noise distribution) by continuously injecting increasing noise using a forward-time Itô stochastic differential equation (SDE),

$$d\mathbf{x} = \mathbf{f}(\mathbf{x}, t)dt + g(t)d\mathbf{w}, \quad (8)$$

also shown at the top of Figure 3. Here, $\mathbf{x} = (\text{Gas}, \text{DM})$ are the gas and dark matter maps, the \mathbf{f} and g components are the drift and diffusion coefficients, and \mathbf{w} is the standard Wiener process. The forward SDE maps $\mathbf{x}(t=0)$ sampled from the data distribution to $\mathbf{x}(t=T)$ sampled from a Gaussian random field.

The model learns to sample the data distribution $p_t(\mathbf{x})$ by solving the reverse-time SDE (e.g. Anderson 1982),

$$d\mathbf{x} = [\mathbf{f}(\mathbf{x}, t) - g^2(t)\nabla_{\mathbf{x}} \log p_t(\mathbf{x})]dt + g(t)d\bar{\mathbf{w}}, \quad (9)$$

which inverts the forward-time transformation by mapping $\mathbf{x}(t=T)$ to $\mathbf{x}(t=0)$, also shown at the bottom of Figure 3. During training, the model estimates the score ($\nabla_{\mathbf{x}} \log p_t(\mathbf{x})$), or the gradient with respect to the data of the log probability density at some time t , by parameterizing it with a deep network $s_\theta(\mathbf{x}, t)$.

The actual training consists of solving for the optimal θ^* via denoising score matching (e.g. Vincent 2011; Song et al. 2021) by optimizing for the following objective:

$$\theta^* = \arg \min_{\theta} \mathbb{E}_{t, \mathbf{x}(t)} \|s_\theta(\mathbf{x}(t), t) - \nabla_{\mathbf{x}(t)} \log p_t(\mathbf{x}(t))\|_2^2. \quad (10)$$

Here, we are finding the best θ^* such that our deep network s_θ best reconstructs, in the L2-norm, the true score of the distribution in expectation across all $t \in [0, T]$ and all $\mathbf{x}(t)$. In practice, $\nabla_{\mathbf{x}(t)} \log p_t(\mathbf{x}(t))$ is evaluated as the numerical derivative between subsequent noising steps.

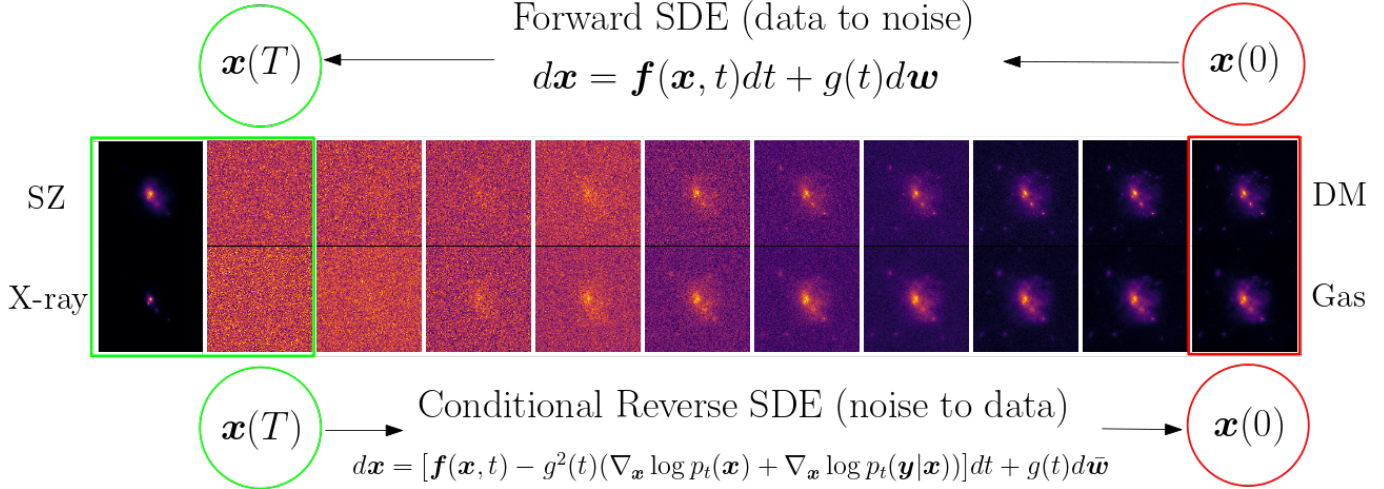


Figure 3. Pedagogical diagram of sampling dark matter (top row) and gas (bottom row) maps using the Euler-Maruyama discretization of Stochastic Differential Equations (SDE), as previously shown in Figure 1 in Song et al. (2021). Before training, we define the forward SDE (top equation), which transforms the data distribution to a random distribution by successively adding noise to the images. During training, the model learns the score of the data distribution in order to sample from it using the conditional reverse SDE (bottom equation), which transforms the random distribution back to the data distribution conditioned on the SZ and X-ray observations (left column). The model utilizes the conditional reverse SDE to generate different realizations of the gas and dark matter maps based on the initial sampled Gaussian random field. The SZ and X-ray inputs along with the initial random samples for the gas and dark matter (green) represent the inputs to our image-to-image diffusion model, while the predicted gas and dark matter (red) represent the outputs.

Finally, a model trained to learn the score from Equation 9 will be able to sample realizations of dark matter and gas maps from a Gaussian random field. However, in our framework we would like to not only learn the distribution of dark matter and gas, but also be able to sample from it conditioned on SZ and X-ray maps, that is, we would like to learn the posterior $p_t(\mathbf{x}|\mathbf{y})$, where $\mathbf{y} = (\text{SZ}, \text{X-ray})$ are the conditional inputs. We can rewrite the reverse SDE to learn a mapping from $p_{t=T}(\mathbf{x}|\mathbf{y})$ to $p_{t=0}(\mathbf{x}|\mathbf{y})$, given by

$$d\mathbf{x} = [\mathbf{f}(\mathbf{x}, t) - g^2(t)(\nabla_{\mathbf{x}} \log p_t(\mathbf{x}) + \nabla_{\mathbf{x}} \log p_t(\mathbf{y}|\mathbf{x}))]dt + g(t)d\bar{\mathbf{w}}, \quad (11)$$

where we learn an additional gradient of the conditional forward process, $\nabla_{\mathbf{x}} \log p_t(\mathbf{y}|\mathbf{x})$, as part of our parameterized network. This will be the actual reverse SDE we use in training.

Our diffusion model uses the Noise Conditional Score Network (NCSN++) architecture and a Variance-Exploding SDE sampling process (VESDE, as described in appendix B of Song et al. 2021) to learn the conditional score of the distribution. The NCSN++ is a variant of RefineNet (Lin et al. 2016), a U-Net variant with instance normalization and dilated convolutions (c.f. Song & Ermon 2019, appendix A). For training, the model has 2 residual blocks per resolution,

and $\sigma_{max} = 1$, the largest intensity of our images, and $\sigma_{min} = 0.001$, which sets the scale of the noise in our images. We use the implementation given by Alexandre Adam’s repository (e.g. Adam et al. 2022; Legin et al. 2023) that can be found at this link: https://github.com/AlexandreAdam/score_models.

4. RESULTS

To validate generated results from our score model, we apply a series of performance metrics to our model with an independent testing set of mock observations. We present sample generated gas and dark matter maps along with their corresponding sampling convergence and fractional standard error (Section 4.1). We then compute the radial density profiles (Section 4.2) and bias and cross correlation coefficients (Section 4.3) and demonstrate that our model is able to generate maps that reconstruct these quantities with high accuracy.

4.1. Mass Maps

The diffusion model is trained on clusters of sizes $1.00 \times 10^{14} \leq M_{200a}/M_{\odot} \leq 4.82 \times 10^{15}$, but we will only test our model on clusters within the range $2.00 \times 10^{14} \leq M_{200a}/M_{\odot} \leq 1.00 \times 10^{15}$ since we lack sufficient data to constrain cluster predictions at these extreme high and low mass tails. Previous deep-learning based estimates of cluster masses (e.g. Ho et al. 2019; Ntampaka et al. 2019; Yan et al. 2020) broadly observed a ‘mean-

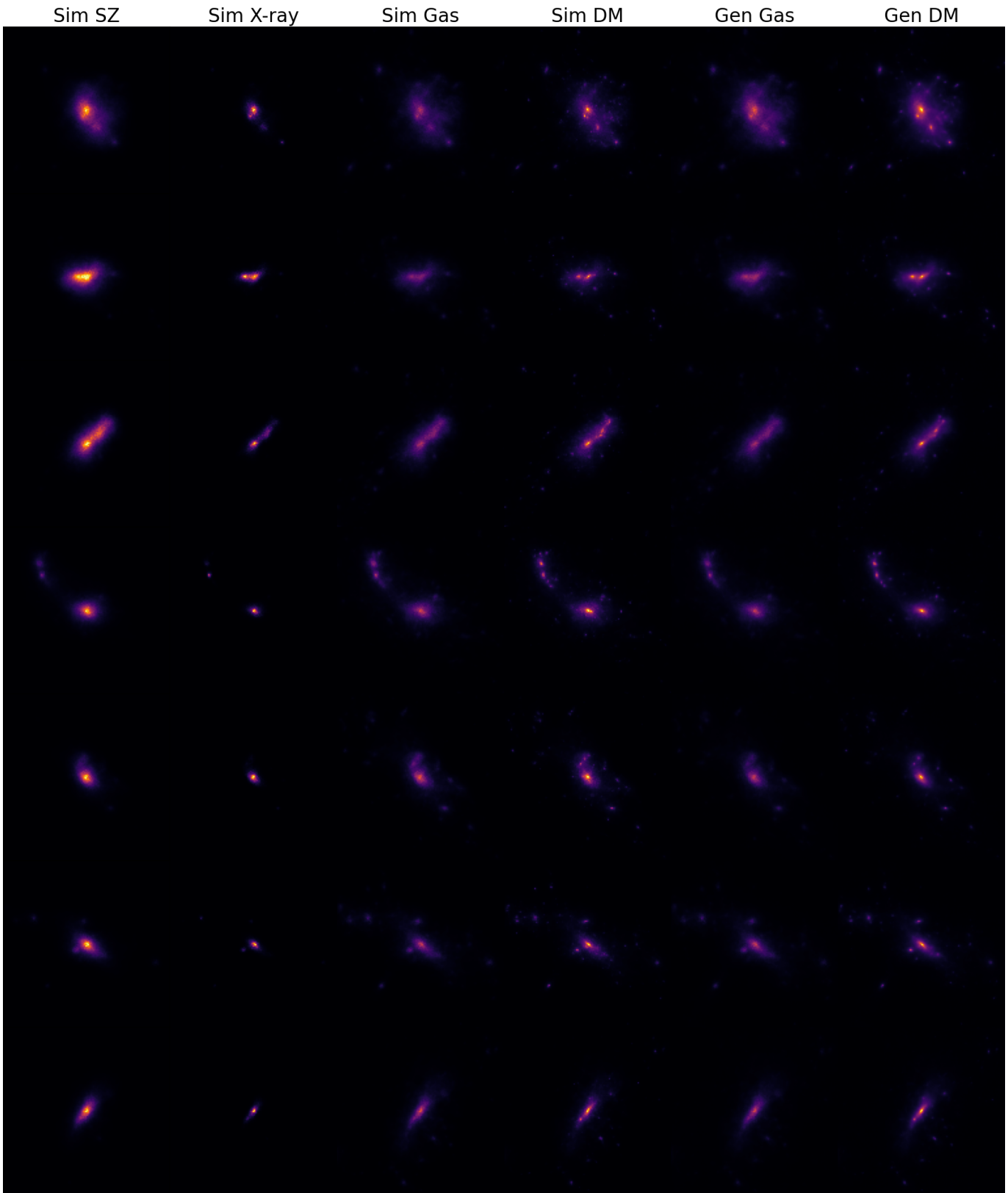


Figure 4. Selected model predictions of gas and dark matter maps (rightmost 2 columns) conditioned on SZ and X-ray inputs (leftmost 2 columns) along with ground truth gas and dark matter maps (middle 2 columns). The predicted maps are averages of 50 samples from the learned joint posterior. Across large and small mass clusters (different rows), we see accurate reconstruction for large and small-scale structures.

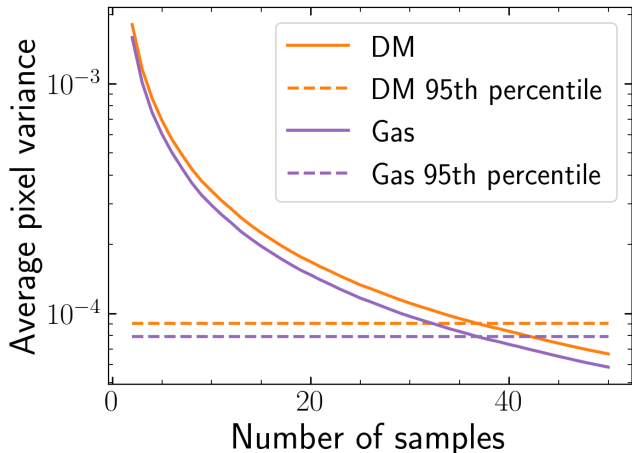


Figure 5. Sample variance of mean pixel gas predictions (purple) and dark matter (orange). Since each starting sample is a different noise realization, the output gas and dark matter maps will be slightly different as well: the sample variance is hence a way of assessing whether the mean of these output images converged. As we increase the number of samples, the variance decreases as we converge to the average value of the posterior distribution: at around 40 samples, the variance goes below the 95th percentile of a 2-sample variance (dotted lines). We thus select 50 samples as a safe threshold when computing our average predictions.

reversion’ effect, wherein the masses of small clusters were overpredicted and those of large clusters were underpredicted. Such effects can be resolved with more training data and broader mass priors. As a result, we exclude these extremities and reserve their analysis for future work. For our test mass region, we will denote clusters within $2.00 \times 10^{14} \leq M_{200a}/M_{\odot} < 6.00 \times 10^{14}$ as low mass clusters and $6.00 \times 10^{14} \leq M_{200a}/M_{\odot} \leq 1.00 \times 10^{15}$ as high mass clusters, roughly divided evenly in log mass space.

The diffusion model samples from the learned posterior by first sampling from a Gaussian random field, and mapping that to a realization of gas and dark matter densities. Since the sampling process is probabilistic, the sample variance is used to determine the number of samples we need from the posterior to produce a converged mean prediction. In Figure 5, we compute the 95th percentile convergence of the sample variance averaged over all pixels, which is around 40 samples for both the gas and dark matter. We will use 50 samples to compute our results.

Figure 4 shows sample galaxy cluster predictions from our diffusion model, with each row being a sample from a different mass bin. The samples are selected to provide a representative overview of the performance of our model on clusters of different shapes and sizes ranging across

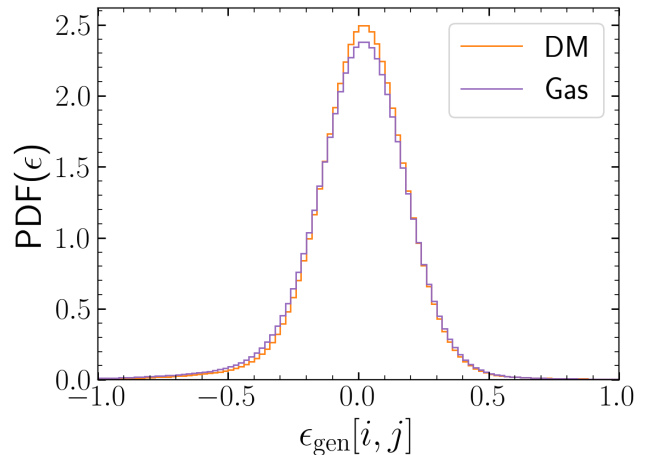


Figure 6. PDF of standardized pixel-wise fractional mass error (Equation 12) of generated gas (purple) and dark matter (orange) maps. The distribution is centered at zero with a smaller-than-normal spread, indicating that our model is under-confident but, on average, unbiased on the pixel level.

our full test mass range. The first 4 columns represent the ground truth simulation maps of SZ, X-ray, gas, and dark matter, respectively. Multiple realizations of the gas and dark matter maps are generated to compute statistical quantities: the final 2 columns represent the generated 50-sample average of the gas and dark matter maps conditioned on the SZ and X-ray inputs. Visually, our model is able to pick up on both the large-scale and small-scale features of the clusters across different mass bins (rows). We further justify the accuracy of our model through statistical metrics.

To understand the bias on a pixel level, we validate our gas and dark matter predictions using a histogram of pixel-level standardized errors ϵ given by the difference between the predicted S_{gen} and the simulated S_{sim} divided by the variance of the predictions σ_{gen} ,

$$\epsilon_{\text{gen}}[i, j] = \frac{S_{\text{gen}}[i, j] - S_{\text{sim}}[i, j]}{\sigma_{\text{gen}}[i, j]}. \quad (12)$$

Figure 6 shows the probability density (normalized histogram) of the error for the gas and dark matter maps, which is approximately normal about zero with a smaller-than-unity spread. As expected, for both mass maps the errors are centered around zero, indicating zero bias during the prediction pipeline of our model on average. However, the spread is much smaller than a standard normal, as 99.5% of the data is contained within $\pm 1\sigma$. Since ϵ_{gen} is computed by dividing by σ_{gen} , the pixel-wise variance of the dark matter and gas maps is actually larger than our posterior variance, indicating that the model is under-confident in its predictions.

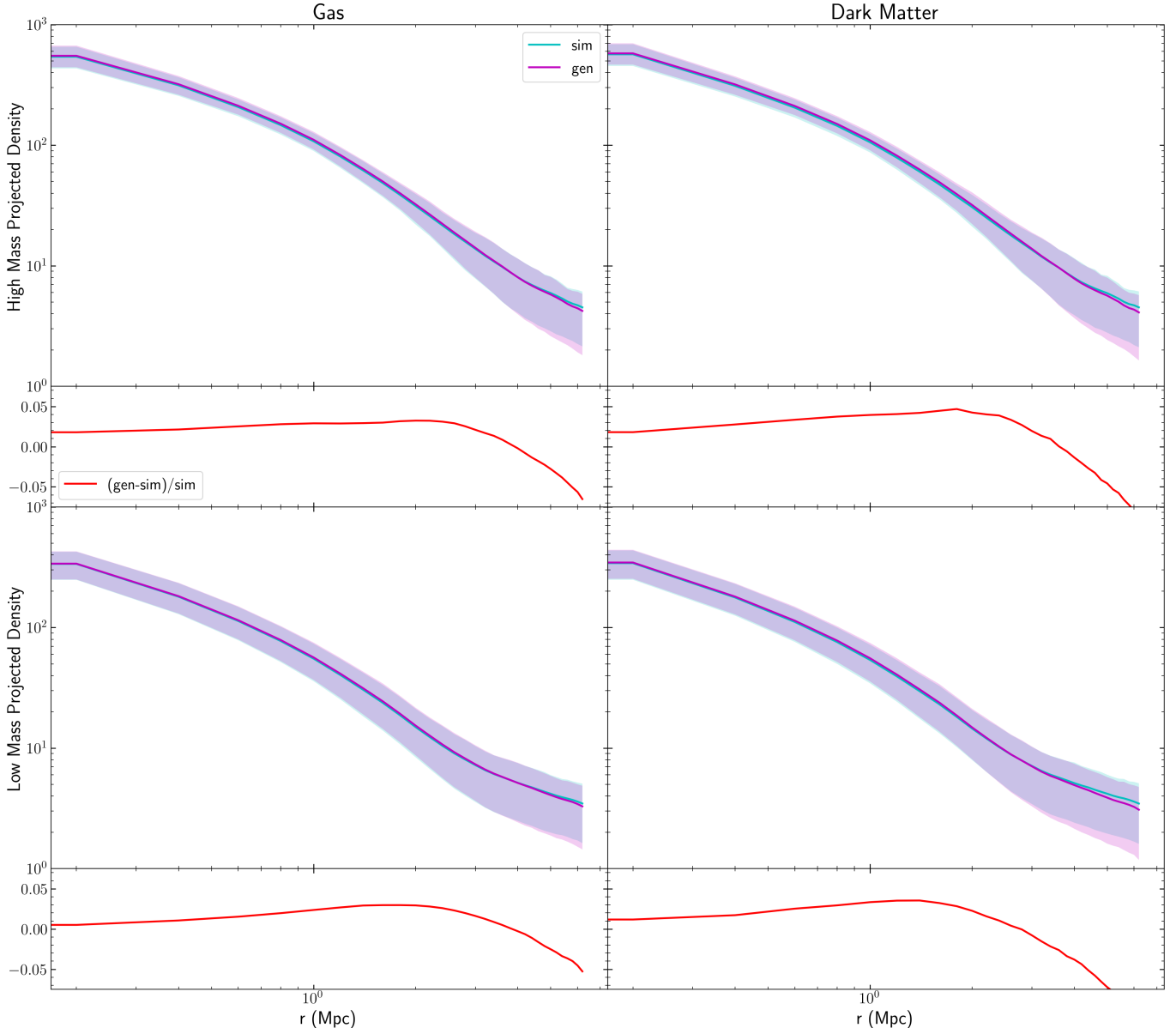


Figure 7. Radial density profiles for dark matter (left) and gas (right). Large cluster profiles are shown on the top, and small cluster profiles are shown on the bottom, and in each panel we graph the generated maps (magenta) and simulated maps (cyan) with the 16th to 84th percentiles shaded. Under each curve, we show the fractional difference between the generated and simulated maps in red, which shows agreement to within 5% across all radial distances. We see that the model slightly overpredicts (positive fractional difference) the cluster density until 3 Mpc, where the fractional difference begins to decline and eventually underpredicts (negative fractional difference). This trend follows the expected behavior to match the zero-density boundary condition of our mass maps.

This metric shows that we did not overfit our model to the training dataset and that the diffusion sampling process does not exhibit mode collapse.

4.2. Density Profiles

To validate the performance of mass reconstruction radially, we compute the average density profile for both the generated and simulated gas and dark matter maps,

binning the pixels radially. Figure 7 shows these profiles on the top panel, along with the associated fractional reconstruction error in the bottom panel. Overall we match both the mean and the 68% spread in our reconstructed mass maps with the ground truth mass distribution, with a 1-2% average fractional error across all clusters in the central $r < 1$ Mpc region, with a slightly larger fractional error but still within 5% at the edge of

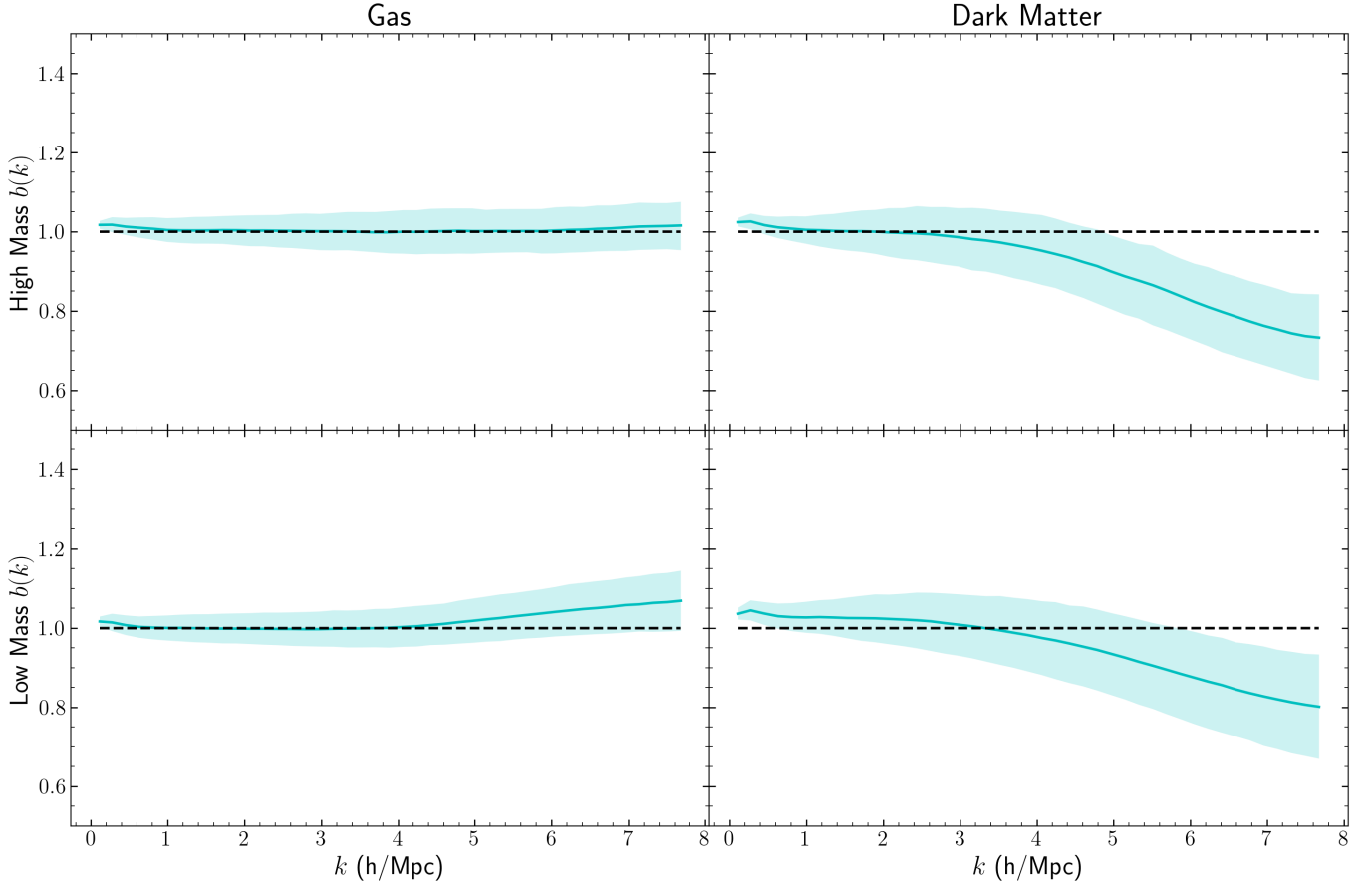


Figure 8. Bias coefficients (blue) between the simulation and generated outputs (Equation 13, for both high mass clusters (top) and low mass clusters (bottom)). The model achieves close-to-unity bias (black) across all scales.

the cluster in regions $r \geq 1$ Mpc. Matching both the mean trend and spread is equally important, as there is natural scatter from the simulation profiles from the various cluster sizes: the fact that our model is able to reproduce this uncertainty is a strong indication that it is able to distinguish between clusters of different sizes.

We further demonstrate that our model tries to preserve the overall mass: the average total mass fractional error for the gas maps is $0.005^{+0.028}_{-0.028}$, while that of the dark matter is $0.008^{+0.023}_{-0.024}$. Thus, the slight over-prediction near the center of the cluster is balanced by the slight under-prediction past the virial radius, where the model is also trying to match the zero boundary condition near the edge of the images. The increase in the magnitude of the error beyond the virial radius is an artifact of the denominator in the fractional error: because there is minimal mass near the edge, the residual (numerator) becomes much larger than the denominator.

Our results improve on the error of those of Figure 6 in de Andres et al. (2024), where they compute the average total mass fractional error of generated density

maps from SZ, X-ray and star observations using a U-Net model to $-0.00^{+0.23}_{-0.18}$. Our model leverages the sampling power of diffusion models to converge to a much more accurate gas and dark matter map rather than a single point estimate as used in other image-to-image models.

4.3. Cross Correlations

In addition to analyzing the spatial reconstruction of our models, we also analyze the accuracy of our results using the bias and cross correlation coefficients in Fourier space. First, the bias is the tendency to under-predict or over-predict pixel intensities in our models, given by the auto-correlation of the simulated maps P_{sim} and the generated maps P_{gen} :

$$b(k) = \sqrt{\frac{P_{\text{gen}}(k)}{P_{\text{sim}}(k)}}. \quad (13)$$

The bias $b(k)$ of a particular channel output is unbiased if $b = 1$, overbiased if $b > 1$, and underbiased if $b < 1$.

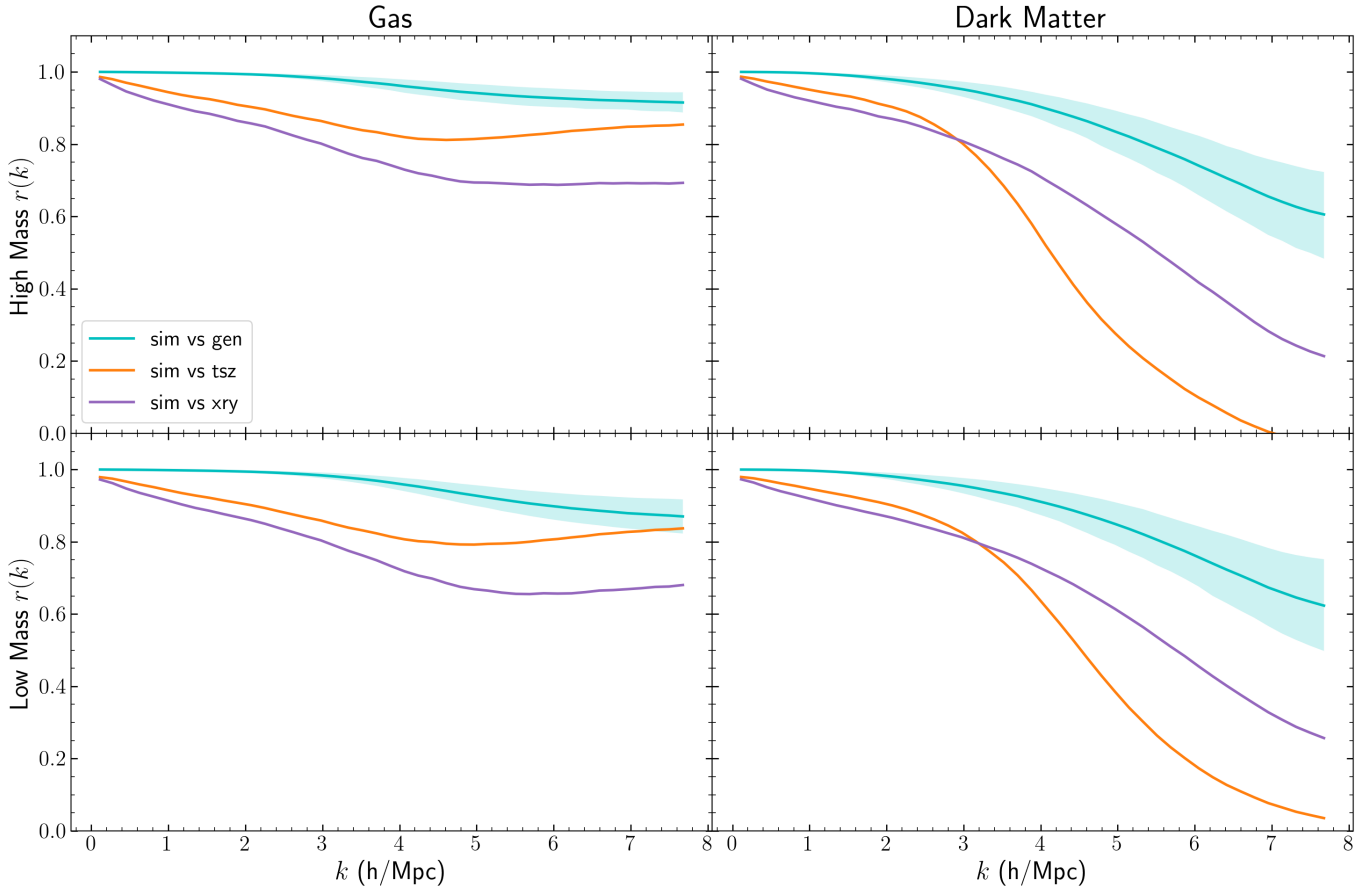


Figure 9. Normalized cross-correlation coefficients between the simulation and generated outputs (blue) of gas (left) and dark matter (right), for both high mass clusters (top) and low mass clusters (bottom). We expect near-perfect agreement of unity on large scales (small k), and a monotonically decreasing behavior as we move to smaller scales (large k). By comparing with the cross-coefficients between the simulated outputs and SZ (orange) and X-ray (purple), we see that our model is able to learn a much stronger nonlinear correlation than that of a scale-dependent linear bias model.

Figure 8 shows the bias coefficients for the simulated outputs and the generated outputs binned radially, assuming angular independence, averaged over all clusters. We see a similar behavior for predicting both high-mass and low-mass clusters. Because our model is learning from mock SZ and X-Ray inputs, which are derived from the simulated gas density, the bias for the generated gas maps is very close to one. For dark matter maps, there is a slight under-bias for small scales, likely because the signal from SZ and X-ray inputs do not fully capture the small-scale structures of the underlying dark matter. In addition, because the gas maps are more smooth in nature, the continuum between large and small scales should be easier to predict compared to dark matter maps.

Second, by computing the normalized cross-correlation coefficients, we can analyze whether or not the generated outputs are better correlated with the simulated outputs than the inputs are with the simu-

lated outputs. Given two mass maps, the normalized cross-correlation is given by

$$r(k) = \frac{P_{\text{sim} \times \text{gen}}(k)}{\sqrt{P_{\text{sim}}(k)P_{\text{gen}}(k)}}, \quad (14)$$

where the numerator is the cross-correlation power spectrum of the two maps and the denominator is the geometric mean of their auto-correlations. The maps are perfectly correlated if $r = 1$, uncorrelated if $r = 0$, and perfectly anti-correlated if $r = -1$.

Figure 9 shows the pairwise cross correlation between the simulated output (ground truth) with the inputs and the generated output in blue. This curve gives us a metric on how well the reconstructed mass maps, across all scales, agree with the simulation mass maps. Plotted in the orange and purple curves are the correlation between the simulated SZ and X-ray inputs with the simulated outputs, respectively, which is a proxy for the best performance a linear bias model can do to map the inputs

Cluster Size	Mass Map	Small scale $b(k)$	Large scale $b(k)$	Small scale $r(k)$	Large scale $r(k)$
high mass	Gas	$1.004^{+0.003}_{-0.005}$	$1.008^{+0.005}_{-0.007}$	$0.949^{+0.028}_{-0.034}$	$0.998^{+0.002}_{-0.002}$
	Dark Matter	$0.888^{+0.115}_{-0.098}$	$1.008^{+0.008}_{-0.011}$	$0.821^{+0.149}_{-0.131}$	$0.994^{+0.006}_{-0.005}$
low mass	Gas	$1.023^{+0.025}_{-0.031}$	$1.004^{+0.005}_{-0.007}$	$0.932^{+0.050}_{-0.052}$	$0.998^{+0.002}_{-0.002}$
	Dark Matter	$0.928^{+0.092}_{-0.081}$	$1.030^{+0.005}_{-0.006}$	$0.832^{+0.143}_{-0.123}$	$0.995^{+0.005}_{-0.005}$

Table 1. Mean bias and cross-correlation values for the generated dark matter and gas maps per scale length bin, dependent on the galaxy cluster size (either high mass or low mass) and the scale length (either $k < 2$ h/Mpc for large scale or $k \geq 2$ h/Mpc for small scales). Across all of these classes, we achieve a close-to-unity bias and high correlation per scale bin using the diffusion model. This indicates that our model is learning a complex, nonlinear mapping between the SZ and X-ray inputs and the dark matter and gas outputs.

to the output mass maps. This effectively serves as a baseline model for mapping the observables to the underlying densities.

For the correlated simulation inputs and outputs, the model behaves similarly for both high-mass and low-mass clusters: the gas is better correlated with the input SZ and X-ray observables than the dark matter since the construction of the gas maps is much more closely aligned with the actual observables than the underlying dark matter maps, which have a much more complex relationship. More specifically, for the gas maps, SZ correlations are stronger than those of X-ray, which agree with Equations 6 and 7: because SZ is proportional to pressure and density while X-ray is proportional to the square of density, we can expect the X-ray signal to be less correlated as the square will be much more sensitive to the small-scale clumpiness of the gas maps. Finally, the diffusion results in blue show that our model is able to learn a much stronger correlation across all scales. [de Andres et al. \(2024\)](#) reconstructs the generated and simulated power spectrum and shows agreement by comparing the relative error, but does not compute $b(k)$ or $r(k)$, which we focus on to show the improvements of our model over linear models in the spectral domain.

In Table 1, we summarize the average values of Figures 8 and 9. Our bias values are in agreement with unity across all scales for both gas and dark matter maps except for high-mass gas maps at the large scale, which is within 0.001 agreement with unity. Our cross-correlation values are close to unity at large scales, and around between 0.8 to 0.95 for small scales, indicating that our model is able to reproduce the structure of clusters very well at these two different scale lengths.

5. CONCLUSION

We present a novel approach to map SZ and X-ray inputs of galaxy clusters to the gas and dark matter density maps using score-based conditional generative models. In particular, our model takes in SZ and X-ray images as conditional inputs, and combines that with a

random sample from a Gaussian random field to produce a corresponding realization of the gas and dark matter maps. Our diffusion model uses Langevin dynamics sampling to generate these maps, wherein the model utilizes the learned score of the data distribution and evolves the noisy image through conditional reverse stochastic differential equations.

We trained our diffusion model using mock SZ and X-ray observations and simulated gas and dark matter densities from HYPER, reserving part of the dataset for downstream testing. During training, the model learns to match the score by reconstructing a gas and dark matter map from a random noisy image sample using the corresponding SZ and X-ray conditional input. As the model optimizes the score over time, it will better reconstruct the score and thus sample better from the posterior, generating more accurate realizations of the gas and dark matter maps.

Our diffusion model is able to generate highly realistic and accurate realizations of gas and dark matter maps. The samples from the model converge since a 50-sample mean is able to achieve a $< 5\%$ 2-sample variance for our test dataset. In addition, because the dataset is normalized by a global maximum and minimum so as to preserve relative intensities between clusters, the model is able to accurately predict the matter distribution across differently-sized clusters. Another indication that our model is able to distinguish between differently-sized clusters is that it is able to reconstruct the mean and spread of both the gas and dark matter density profiles to within 5% on all spatial scales and all cluster sizes. Finally, in the spectral domain, the model achieves a close-to-unity agreement for the bias coefficients and high cross-correlation coefficients between the simulated and generated density maps, implying that our model learns a strong nonlinear mapping that can accurately probe both large and small scale cluster structures.

Future work can be done to improve the reconstruction of the mass maps in both the spatial and spectral

domains. Currently, our loss is only the score-matching term, which does not include any information on the physical constraints of our data. We can utilize physics-informed losses during learning, where we augment our loss with extra terms, such as constraints on the total mass of the cluster or regularization terms on the bias and cross-correlation coefficients at different scale lengths. Improvements can also be made on the data end: by adding structured noise to our dataset, we can increase the robustness of our model towards imperfect observations.

The success of our diffusion model to accurately predict gas and dark matter realizations by sampling from a learned distribution has huge implications in real-data inference: our model can be eventually fine-tuned and generalized to not only take in real SZ and X-ray observables, but also additional channels such as weak lensing measurements that can provide more insight towards the

internal cluster dynamics. These diffusion models can ultimately be used to predict unknown gas and dark matter distributions of real galaxy clusters of interest.

¹ We thank Jun-Yan Zhu for discussions on generative
² modeling, and Nick Gnedin, Yuuki Omori, and Qirong
³ Zhu for discussions on HYPER. We also thank Alexan-
⁴ dre Adam for making his implementation of score mod-
⁵ els publicly available. Finally, we thank Ashley Villar
⁶ for guidance on parts of this project during the Spring
⁷ 2024 ASTRON205 course at Harvard University. The
⁸ HYPER simulation was run on Endeavour at the NASA
⁹ Advanced Supercomputing (NAS) Division. The ma-
¹⁰ chine learning work was run on the FASRC Cannon
¹¹ cluster supported by the FAS Division of Science Re-
¹² search Computing Group at Harvard University. This
¹³ project is supported by NASA grant 80NSSC22K0821.

REFERENCES

- Adam, A., Coogan, A., Malkin, N., et al. 2022, arXiv e-prints, doi: [10.48550/arXiv.2211.03812](https://doi.org/10.48550/arXiv.2211.03812)
- Aghanim, N., Arnaud, M., Ashdown, M., et al. 2011, *Astronomy & Astrophysics*, 536, A26
- Allen, S. W., Evrard, A. E., & Mantz, A. B. 2011, *ARA&A*, 49, 409, doi: [10.1146/annurev-astro-081710-102514](https://doi.org/10.1146/annurev-astro-081710-102514)
- Allen, S. W., Schmidt, R., & Fabian, A. 2002, *Monthly Notices of the Royal Astronomical Society*, 335, 256
- Anderson, B. D. 1982, *Stochastic Processes and their Applications*, 12, 313, doi: [https://doi.org/10.1016/0304-4149\(82\)90051-5](https://doi.org/10.1016/0304-4149(82)90051-5)
- Arendt, A. R., Perrott, Y. C., Contreras-Santos, A., et al. 2024, *Monthly Notices of the Royal Astronomical Society*, 530, 20, doi: [10.1093/mnras/stae568](https://doi.org/10.1093/mnras/stae568)
- Bahar, Y. E., Bulbul, E., Clerc, N., et al. 2022, *Astronomy & Astrophysics*, 661, A7
- Barnes, D. J., Vogelsberger, M., Pearce, F. A., et al. 2021, *MNRAS*, 506, 2533, doi: [10.1093/mnras/stab1276](https://doi.org/10.1093/mnras/stab1276)
- Bleem, L. E., Klein, M., Abbot, T. M. C., et al. 2024, *The Open Journal of Astrophysics*, 7, 13, doi: [10.21105/astro.2311.07512](https://doi.org/10.21105/astro.2311.07512)
- Böhringer, H., Schuecker, P., Pratt, G. W., et al. 2007, *A&A*, 469, 363, doi: [10.1051/0004-6361:20066740](https://doi.org/10.1051/0004-6361:20066740)
- Bourdin, A., Legin, R., Ho, M., et al. 2024, arXiv preprint arXiv:2408.00839
- Cohn, J. D., & Battaglia, N. 2019, *MNRAS*, 491, 1575, doi: [10.1093/mnras/stz3087](https://doi.org/10.1093/mnras/stz3087)
- Dehnen, W., & Aly, H. 2012, *MNRAS*, 425, 1068, doi: [10.1111/j.1365-2966.2012.21439.x](https://doi.org/10.1111/j.1365-2966.2012.21439.x)
- de Andres, D., Cui, W., Yepes, G., et al. 2024, *Monthly Notices of the Royal Astronomical Society*, 528, 1517, doi: [10.1093/mnras/stae071](https://doi.org/10.1093/mnras/stae071)
- Doorenbos, L., Cavuoti, S., Longo, G., et al. 2022, arXiv e-prints, arXiv:2211.05556, doi: [10.48550/arXiv.2211.05556](https://doi.org/10.48550/arXiv.2211.05556)
- Doorenbos, L., Sestl, E., Heng, K., et al. 2024, arXiv e-prints, arXiv:2406.18175, doi: [10.48550/arXiv.2406.18175](https://doi.org/10.48550/arXiv.2406.18175)
- Ettori, S., Ghirardini, V., Eckert, D., et al. 2019, *Astronomy & Astrophysics*, 621, A39
- Giles, P., Maughan, B. J., Bonamente, M., et al. 2017, *MNRAS*, 465, 858, doi: [10.1093/mnras/stw2621](https://doi.org/10.1093/mnras/stw2621)
- Gnedin, N. Y., & Hui, L. 1998, *MNRAS*, 296, 44, doi: [10.1046/j.1365-8711.1998.01249.x](https://doi.org/10.1046/j.1365-8711.1998.01249.x)
- Green, S. B., Ntampaka, M., Nagai, D., et al. 2019, *ApJ*, 884, 33, doi: [10.3847/1538-4357/ab426f](https://doi.org/10.3847/1538-4357/ab426f)
- Han, Z., Mead, A. J., Waerbeke, L. V., Hinshaw, G., & McCarthy, I. G. 2020, *MNRAS*, 499, 3445, doi: [10.1093/mnras/staa3030](https://doi.org/10.1093/mnras/staa3030)
- He, Y., Mansfield, P., Rau, M. M., Trac, H., & Battaglia, N. 2021, *ApJ*, 908, 91, doi: [10.3847/1538-4357/abd0ff](https://doi.org/10.3847/1538-4357/abd0ff)
- He, Y., Trac, H., & Gnedin, N. Y. 2022, *ApJ*, 925, 134, doi: [10.3847/1538-4357/ac3bcb](https://doi.org/10.3847/1538-4357/ac3bcb)
- Hemmati, S., Huff, E., Nayyeri, H., et al. 2022, *ApJ*, 941, doi: [10.3847/1538-4357/aca1b8](https://doi.org/10.3847/1538-4357/aca1b8)
- Hilton, M., Sifón, C., Naess, S., et al. 2021, *ApJS*, 253, 3, doi: [10.3847/1538-4365/abd023](https://doi.org/10.3847/1538-4365/abd023)

- Ho, J., Jain, A., & Abbeel, P. 2020, in *Advances in Neural Information Processing Systems*, ed. H. Larochelle, M. Ranzato, R. Hadsell, M. Balcan, & H. Lin, Vol. 33 (Curran Associates, Inc.), 6840–6851
- Ho, M., Farahi, A., Rau, M. M., & Trac, H. 2021, *ApJ*, 908, 204, doi: [10.3847/1538-4357/abd101](https://doi.org/10.3847/1538-4357/abd101)
- Ho, M., Ntampaka, M., Rau, M. M., et al. 2022, *Nature Astronomy*, 6, 936, doi: [10.1038/s41550-022-01711-1](https://doi.org/10.1038/s41550-022-01711-1)
- Ho, M., Rau, M. M., Ntampaka, M., et al. 2019, *ApJ*, 887, 25, doi: [10.3847/1538-4357/ab4f82](https://doi.org/10.3847/1538-4357/ab4f82)
- Ho, M., Soltis, J., Farahi, A., et al. 2023, arXiv, doi: [10.48550/arXiv.2303.00005](https://doi.org/10.48550/arXiv.2303.00005)
- Illani, G., Hou, K.-C., Nadler, G., & Keshet, U. 2024, *Astronomy & Astrophysics*, 686, L16
- Kay, S. T., Peel, M. W., Thomas, P. A., et al. 2012, *MNRAS*, 422, 1999, doi: [10.1111/j.1365-2966.2012.20623.x](https://doi.org/10.1111/j.1365-2966.2012.20623.x)
- Kodi Ramanah, D., Wojtak, R., Ansari, Z., Gall, C., & Hjorth, J. 2020, *MNRAS*, 499, 1985, doi: [10.1093/mnras/staa2886](https://doi.org/10.1093/mnras/staa2886)
- Kodi Ramanah, D., Wojtak, R., & Arendse, N. 2021, *MNRAS*, 501, 4080, doi: [10.1093/mnras/staa3922](https://doi.org/10.1093/mnras/staa3922)
- Kravtsov, A. V., & Borgani, S. 2012, *ARA&A*, 50, 353, doi: [10.1146/annurev-astro-081811-125502](https://doi.org/10.1146/annurev-astro-081811-125502)
- Kravtsov, A. V., Vikhlinin, A., & Nagai, D. 2006, *ApJ*, 650, doi: [10.1086/506319](https://doi.org/10.1086/506319)
- Legin, R., Adam, A., Hezaveh, Y., & Perreault-Levasseur, L. 2023, *ApJL*, 949, L41, doi: [10.3847/2041-8213/acd645](https://doi.org/10.3847/2041-8213/acd645)
- Legin, R., Ho, M., Lemos, P., et al. 2023, *Monthly Notices of the Royal Astronomical Society: Letters*, 527, L173, doi: [10.1093/mnrasl/slاد152](https://doi.org/10.1093/mnrasl/slاد152)
- Li, Y., Ni, Y., Croft, R. A. C., et al. 2021, *Proceedings of the National Academy of Sciences (PNAS)*, 118, doi: [10.1073/pnas.2022038118](https://doi.org/10.1073/pnas.2022038118)
- Lin, G., Milan, A., Shen, C., & Reid, I. 2016, *RefineNet: Multi-Path Refinement Networks for High-Resolution Semantic Segmentation*. <https://arxiv.org/abs/1611.06612>
- Lovisari, L., Forman, W. R., Jones, C., et al. 2017, *The Astrophysical Journal*, 846, 51
- Mantz, A. B., Allen, S. W., Morris, R. G., et al. 2016, *MNRAS*, 463, 3582, doi: [10.1093/mnras/stw2250](https://doi.org/10.1093/mnras/stw2250)
- Marriage, T. A., Acquaviva, V., Ade, P. A. R., et al. 2011, *ApJ*, 737, 61, doi: [10.1088/0004-637X/737/2/61](https://doi.org/10.1088/0004-637X/737/2/61)
- Melin, J. B., Bartlett, J. G., Tarrío, P., & Pratt, G. W. 2021, *A&A*, 647, A106, doi: [10.1051/0004-6361/202039471](https://doi.org/10.1051/0004-6361/202039471)
- Nguyen, T., Villaescusa-Navarro, F., Mishra-Sharma, S., et al. 2024, arXiv e-prints, arXiv:2409.02980, doi: [10.48550/arXiv.2409.02980](https://doi.org/10.48550/arXiv.2409.02980)
- Ntampaka, M., Trac, H., Sutherland, D. J., et al. 2015, *ApJ*, 803, 50, doi: [10.1088/0004-637X/803/2/50](https://doi.org/10.1088/0004-637X/803/2/50)
- Ntampaka, M., ZuHone, J., Eisenstein, D., et al. 2019, *ApJ*, 876, 82, doi: [10.3847/1538-4357/ab14eb](https://doi.org/10.3847/1538-4357/ab14eb)
- Perraudin, N., Srivastava, A., Lucchi, A., et al. 2019, *Computational Astrophysics and Cosmology*, 6, doi: doi.org/10.1186/s40668-019-0032-1
- Pratt, G., Croston, J. H., Arnaud, M., & Bohringer, H. 2009, *Astronomy & Astrophysics (A&A)*, 498, 361, doi: [10.1051/0004-6361/200810994](https://doi.org/10.1051/0004-6361/200810994)
- Reddy, P., Toomey, M. W., Parul, H., & Gleyzer, S. 2024, arXiv e-prints, arXiv:2406.08442, doi: [10.48550/arXiv.2406.08442](https://doi.org/10.48550/arXiv.2406.08442)
- Reichardt, C. L., Stalder, B., Bleem, L. E., et al. 2013, *ApJ*, 763, 127, doi: [10.1088/0004-637X/763/2/127](https://doi.org/10.1088/0004-637X/763/2/127)
- Rodriguez, A., Kacprzak, T., Lucchi, A., et al. 2018, *Computational Astrophysics and Cosmology*, 5, doi: [10.1186/s40668-018-0026-4](https://doi.org/10.1186/s40668-018-0026-4)
- Sarazin, C. L. 1988, *S&T*, 76, 639
- Schawinski, K., Turp, M. D., & Zhang, C. 2018, *Astronomy & Astrophysics (A&A)*, 616, doi: [10.1051/0004-6361/201833800](https://doi.org/10.1051/0004-6361/201833800)
- Schawinski, K., Zhang, C., Zhang, H., Fowler, L., & Sathanam, G. K. 2017, *MNRAS*, 467, L110, doi: [10.1093/mnrasl/slx008](https://doi.org/10.1093/mnrasl/slx008)
- Sohl-Dickstein, J., Weiss, E. A., Maheswaranathan, N., & Ganguli, S. 2015, *CoRR*, abs/1503.03585
- Song, Y., & Ermon, S. 2019, *CoRR*, abs/1907.05600
- Song, Y., Sohl-Dickstein, J., Kingma, D. P., et al. 2021, in *International Conference on Learning Representations*. <https://openreview.net/forum?id=PxtIG12RRHS>
- Springel, V. 2010, *ARA&A*, 48, 391, doi: [10.1146/annurev-astro-081309-130914](https://doi.org/10.1146/annurev-astro-081309-130914)
- Sunyaev, R. A., & Zeldovich, Y. B. 1970, *Comments on Astrophysics and Space Physics*, 2, 66
- . 1972, *Comments on Astrophysics and Space Physics*, 4, 173
- Trac, H., Cen, R., & Mansfield, P. 2015, *ApJ*, 813, 54, doi: [10.1088/0004-637X/813/1/54](https://doi.org/10.1088/0004-637X/813/1/54)
- Ullmo, M., Decelle, A., & Aghanim, N. 2021, *Astronomy & Astrophysics (A&A)*, 651, doi: [10.1051/0004-6361/202039866](https://doi.org/10.1051/0004-6361/202039866)
- Vikhlinin, A., Kravtsov, A., Forman, W., et al. 2006, *ApJ*, 640, 691, doi: [10.1086/500288](https://doi.org/10.1086/500288)
- Vikhlinin, A., Burenin, R., Ebeling, H., et al. 2009, *The Astrophysical Journal*, 692, 1033
- Vincent, P. 2011, *Neural Computation*, 23, 1661, doi: [10.1162/NECO_a.00142](https://doi.org/10.1162/NECO_a.00142)
- Wadekar, D., Thiele, L., Hill, J. C., et al. 2023a, *MNRAS*, 522, 2628, doi: [10.1093/mnras/stad1128](https://doi.org/10.1093/mnras/stad1128)

Wadekar, D., Thiele, L., Villaescusa-Navarro, F., et al.
2023b, Proceedings of the National Academy of Sciences
(PNAS), 120, 12, doi: [10.1073/pnas.2202074120](https://doi.org/10.1073/pnas.2202074120)

Yan, Z., Mead, A., Van Waerbeke, L., Hinshaw, G., &
McCarthy, I. 2020, Monthly Notices of the Royal
Astronomical Society, 499, 3445

Zwicky, F. 1933, Helvetica Physica Acta, 6, 110